Assessing the Ducting Phenomenon and its Potential Impact on GNSS Radio Occultation Refractivity Retrievals over the Northeast Pacific Ocean using Radiosondes and Global Reanalysis

Thomas E. Winning Jr.[1], Feiqin Xie[1] and Kevin J. Nelson[1,a]

[1] Texas A&M University – Corpus Christi, Corpus Christi, 78412, USA

[a] now at: Jet Propulsion Laboratory, California Institute of Technology, Pasadena, 91109, USA

Correspondence to: Thomas E. Winning Jr. (twinning@islander.tamucc.edu)

Abstract. In this study, high-resolution radiosondes from the MAGIC field campaign and ERA5 global reanalysis data are used to assess characteristics of the elevated ducting layer along a transect over the northeastern Pacific Ocean from Los Angeles, California to Honolulu, Hawaii. The planetary boundary layer (PBL) height (PBLH) increases as the strength of the refractivity gradient decreases westward along the transect. The thickness of the prevailing ducting layer remains remarkably consistent (~110 m) in the radiosonde data. On the other hand, the ERA5 reanalysis generally resolves the ducting features well, but underestimates the ducting height and strength, especially over the trade cumulus region near Hawaii. A simple two-step end-to-end simulation is used to evaluate the impact of the elevated ducting layer on RO refractivity retrievals. A systematic negative refractivity bias (N-bias) below the ducting layer is observed throughout the transect, peaking (-5.42%) slightly below the PBLH, and gradually decreasing towards the surface (-0.5%). The N-bias shows strong positive correlation with the ducting strength. The ERA5 data underestimate the N-bias with the magnitude of the underestimation increasing westward along the transect.

1 Introduction

The troposphere, where most weather occurs, consists of two main layers: the planetary boundary layer (PBL) and the free atmosphere (FA) (Garratt, 1994). The PBL characteristics change frequently on both spatial and temporal scales and the PBL height (PBLH) can impact the exchange of heat, momentum, and particulate matter with the FA, making it a critical factor in global energy balances and water cycling (Stull 1988; Ramanathan et al. 1989; Klein and Hartmann 1993). Regular PBL observations are mainly limited to in-situ measurements from surface stations and radiosondes. However, spatially and temporally dense in-situ PBL observations are typically only available from field campaigns such as the Boundary Layer Experiment 1996 (BLX96, Stull et al. 1997), the Variability of the American Monsoon Systems (VAMOS) Ocean-Cloud-Atmosphere-Land Study Regional Experiment (VOCALS-REx, Wood et al. 2011), and the Marine Atmospheric Radiation Measurement (ARM) Global Energy and Water Experiment (GEWEX) Cloud System Studies (GCSS) Pacific Cross Section Intercomparison (GPCI) Investigation of Clouds (MAGIC, Zhou et al. 2015). Satellite observations of the PBL are also limited due to signal attenuation of the conventional infrared sounder in the lower troposphere and the low vertical resolution of microwave sounding instruments. Additionally, while the depth of the PBLH can vary from a couple hundred meters to a few kilometers (Ao et al. 2012; von Engeln and Teixeira 2013), the transition layer from the PBL to the FA is typically on the order of tens to hundreds of meters thick (Maddy and Barnet 2008), rendering PBL sensing from the low vertical resolution passive infrared and microwave sounders ineffective.

On the other hand, Global Navigation Satellite System (GNSS) radio occultation (RO) provides global atmospheric soundings with a vertical resolution of approximately 100 m in the lower troposphere under all weather conditions (Kursinski et al., 1997, 2000; Gorbunov et al., 2004). Some of the recent major GNSS RO missions are the Formosat-3/Constellation Observing System for Meteorology, Ionosphere, and Climate (COSMIC), later referred to as COSMIC-1 (Anthes et al. 2008), and its follow-on mission COSMIC-2 (Schreiner et al. 2020). Numerous studies have documented the high value of GNSS RO for profiling the PBL and determining the PBLH (Ao et al. 2008; Xie et al. 2008; Basha and Ratnam 2009; Guo et al. 2011; Ao et al. 2012; Ho et al. 2015; Winning et al. 2017; Nelson et al. 2021).

The advancement of the GNSS RO technique with open-loop tracking (Ao et al., 2003; Beyerle et al., 2003; Sokolovskiy et al., 2006) along with the implementation of radio-holographic retrieval algorithms (Gorbunov, 2002; Jensen et al., 2003; Jensen et al., 2004) have led to much-improved PBL sounding quality. However, probing the marine PBL remains challenging, as systematic negative biases are frequently seen in RO refractivity retrievals (Xie et al. 2010; Feng et al. 2020). One major cause of refractivity bias (hereafter N-bias) is the RO retrieval error due to elevated atmospheric ducting often seen near the PBLH (Sokolovskiy 2003; Ao et al. 2003; Xie et al., 2006; Ao et al., 2007). This elevated ducting is found primarily over the subtropical eastern oceans (von Englen et al., 2003; Lopez, 2009; Feng et al., 2020), and the horizontal extent of ducting in these regions can be on the order of thousands of kilometers (Xie et al. 2010; Winning et al. 2017). In the presence of ducting, the vertical refractivity gradient exceeds the critical refraction threshold for L-band frequencies (i.e., $dN/dz \leq -157$ N-units km^{-1}). The steep negative refractivity gradient is often observed in the vicinity of the PBLH, which is typically caused by an atmospheric temperature inversion, a sharp decrease in moisture, or a combination of both. When ducting is present, the Abel inversion (e.g., Fjeldbo et al., 1971) in the standard RO retrieval process encounters a non-unique inversion problem due to a singularity in the bending angle, resulting in large, systematic underestimation of refractivity (N) below the ducting layer (Ao et al., 2003; Sokolovskiy, 2003; Xie et al. 2006). The large uncertainty in RO refractivity coupled with the singularity in bending angle hinders assimilation of RO observations into numerical weather models, resulting in the rejection of a significant percentage of RO measurements inside the PBL (Healy, 2001).

To comprehensively assess the potential impact of ducting on GNSS RO retrievals, we begin by constructing a detailed ground truth of PBL ducting statistics. This is derived from an extensive set of high-resolution radiosonde data over the northeastern Pacific Ocean, a region known for prevailing ducting conditions. Subsequently, we conduct a simulation study using the radiosonde data to evaluate the N-biases caused by varying ducting characteristics. Section 2 provides details of the two data sets used for this study: high-resolution radiosondes over the northeastern Pacific Ocean and the colocated ECMWF Reanalysis version 5 (ERA5, Hersbach et al. 2020) profiles. Additionally, we discuss the colocation criteria and the detection method for ducting layer and the corresponding PBLH. Section 3 presents the ducting statistics for key variables, such as ducting height, PBLH, minimum refractivity gradient, and sharpness parameter. The characteristics of

91 ducting including the thickness and strength along the cross-section are also shown. Furthermore,

92 we evaluate the ducting-induced *N*-bias in GNSS RO refractivity retrievals by carrying out a two-

93 step end-to-end simulation. Section 4 summarizes the findings and discusses the direction of future

94 research.

95 **2   Data and methods**

96 **2.1 MAGIC radiosonde and colocated ERA5 data**

97 A collection of high-resolution radiosondes from the Marine Atmospheric Radiation Measurement

98 (ARM) GCSS Pacific Cross Section Intercomparison (GPCI) Investigation of Clouds (MAGIC)

99 are utilized as the primary data set in this analysis (Zhou et al. 2015; Lewis 2016). The MAGIC

100 field campaign took place from 26 September 2012 to 2 October 2013 as part of the U.S

101 Department of Energy ARM Program Mobile Facility 2 (AMF2) aboard the Horizon Lines

102 container ship, *Spirit*, which completed 20 round trip passes between Los Angeles, California and

103 Honolulu, Hawaii during the yearlong data collection period (Painemal et al., 2015; Zhou, 2015).

104 During each transit, radiosondes were launched at 6-hour intervals from the beginning of the

105 program through the end of June 2013; the observation frequency increased to every 3 hours from

106 July 2013 through the end of the campaign (Zhou et al., 2015). A total of 583 MAGIC radiosonde

107 profiles were collected during the field campaign (Zhou et al., 2015), all with a vertical sampling

108 frequency of 0.5 Hz (2 seconds), which provides an average vertical resolution of ~8 m below 3

109 km, but varies due to local vertical motion.

110 Use of this data set serves multiple benefits. First, the northeast Pacific transitions from a shallow

111 stratocumulus-topped PBL to a deeper, trade-cumulus boundary layer regime along the GPCI

112 transect shown in Figure 1 (Garratt, 1994). Second, the large number of observations over a 12-

113 month time frame provides high temporal (diurnal- and seasonal-scale) and spatial profiling of the

114 PBL along the GPCI transect (Fig. 1). Finally, ducting is prevalent throughout the domain over

115 which the observations were captured creating an opportunity to perform an analysis over a natural

116 cross-section of X (zonal) and Z (vertical) dimensions.
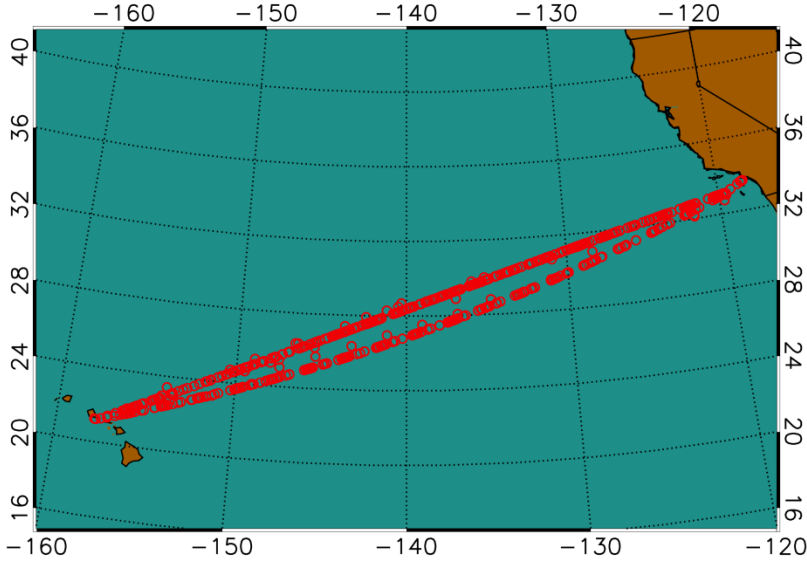
Figure 1: Location of radiosonde observations from the MAGIC field campaign October 2012–September 2013.

The radiosonde profiles are colocated with ERA5 model profiles for this analysis. The ERA5 data have a horizontal resolution of 0.25°x0.25°, 137 non-equidistant vertical model levels from the surface to 0.01 hPa, and 1-hour temporal resolution. The model level density decreases with height: on average, there are 19 model levels below 1 km (10 –100 m resolution), which reduces to 8 levels between 1 and 2 km (100 – 160 m resolution), and further reduces to 5 levels between 2 and 3 km (160-200 m resolution). Each MAGIC radiosonde profile was colocated with the nearest ERA5 grid point that is within 1.5 hours of the closest 3-hourly model profile.

2.2 PBLH detection with the minimum gradient method

At GNSS L-band frequencies, the atmospheric refractivity (N in N-units) is derived from the refractive index n, where $N = (n - 1) \times 10^6$ and, in the neutral atmosphere (Kursinski et al., 1997), is a function of the atmospheric pressure (P in mb), temperature (T in K), and partial pressure of water vapor (P_w in mb) as seen in Eq. (1) from Smith and Weintraub (1953).

$$N = 77.6 \frac{P}{T} + 3.73 \times 10^5 \frac{P_w}{T^2},\tag{1}$$

Over the subtropical eastern oceans, a sharp decrease in moisture is often associated with a strong temperature inversion marking a clear transition from the PBL to the FA. The distinct decrease in moisture and the temperature inversion leads to a sharp negative refractivity gradient which can be precisely detected from GNSS RO. Numerous studies have implemented the simple gradient method to detect the PBLH, i.e., the height of the minimum refractivity gradient (Xie et al., 2006;

138   Seidel et al., 2010; Ao et al., 2012). To assess the robustness of the PBLH detection with the

139   gradient method, Ao et al. (2012) introduced the sharpness parameter ($\widetilde{N}'$) to measure the relative

140   magnitude of the minimum gradient, which is defined as the ratio of the minimum vertical

141   refractivity gradient (N'_{min}) to the root mean square (N'_{RMS}) of the refractivity gradient profile from

142   surface to 5 km as follows.

143    $$\widetilde{N}' \equiv -\frac{N'_{min}}{N'_{RMS}}, \tag{2}$$

144   In this study, the MAGIC radiosonde refractivity profiles were first interpolated to a uniform 10

145   m vertical grid and then smoothed by a 100 m boxcar window to reduce the noise in the gradient

146   profile resulting from the high sampling rate. Moreover, the 100 m smoothed radiosonde will be

147   more consistent with the vertical resolution of GNSS RO measurements (e.g., Gorbunov et al.,

148   2004). Colocated ERA5 data were also vertically interpolated to the same 10 m grid but not

149   smoothed as these data do not contain the inherent noise as the radiosonde observations. In the

150   case of both data sets, quadratic interpolation is used to translate the refractivity profiles from their

151   native height values to a uniform height. Finally, as the elevated ducting layer is the focus of this

152   study, the lowest 0.3 km above mean-sea-level of the N-profile are excluded (e.g., Xie et al., 2012).

153   Subsequently, the height of the minimum refractivity gradient (within 0.3 km and 5 km) will be

154   identified as the PBLH.

155   **2.3 Ducting layers**

156   The refractivity gradient profile is calculated by differentiating the 10 m interpolated refractivity

157   profile with respect to height. When the vertical refractivity gradient is less than the critical

158   refraction threshold for radio waves ($dN/dz < -157.0$ N-units km^{-1}), ducting occurs (Sokolovskiy,

159   2003). A ducting layer is identified as any interval of continuous points with a vertical refractivity

160   gradient equal to or less than the critical refraction threshold. Instances of multiple ducting layers

161   occurring within a profile are present for both the MAGIC (31.5%) and ERA5 (6.7%) data sets. In

162   this study, we only recognize one dominant "ducting layer" in each profile where the minimum

163   vertical gradient is located. The ducting layer thickness (Δh) is defined as the interval between the

164   top and bottom of the ducting layer where the refractivity gradients reach critical refraction.

165   Similarly, the strength of each ducting layer (ΔN) is defined as the refractivity difference between

166   the bottom and top of the ducting layer. The ducting layer height is defined as the height of the top

167   of the ducting layer (Ao, 2007), which is generally slightly above the PBLH.

168   Figure 2 shows vertical profiles of refractivity (N in da$N$-units), temperature (T in ˚C), and specific

169   humidity (q in g/kg) along with their respective vertical gradients (dN/dz, dT/dz, and dq/dz) from

170   a representative MAGIC radiosonde (Fig. 2a,b) case located at (23.69˚, −150.02˚), and its

171   colocated ERA5 (Fig. 2c,d) profile at (23.75˚, −150.00˚). The PBLH of the radiosonde (2.10 km)

172   is almost identical to the colocated ERA5 (2.14 km) and the "dominant" ducting layer near the

173   PBLH demonstrates similar thickness. However, a second, weaker ducting layer seen in the

174   radiosonde above the PBLH was not captured by the ERA5. It should be noted that the weak "saw

175   tooth-like" gradients seen above the minimum in the ERA5 refractivity gradient (Fig. 2d) are a

176   result of the vertical derivative being calculated from the interpolated ERA5 refractivity profile.

177   When interpolating the relatively coarse vertical resolution ERA5 profile (up to 200 m in the

178   lowest 3 km) into 10 m vertical sampling, the higher-order interpolation could lead to fine structure

179   in the first order derivative. However, these minor gradients only marginally affect the estimates

180   of minimum gradient and associated heights from ERA5 and is most often overshadowed by the

181   PBLH gradient.
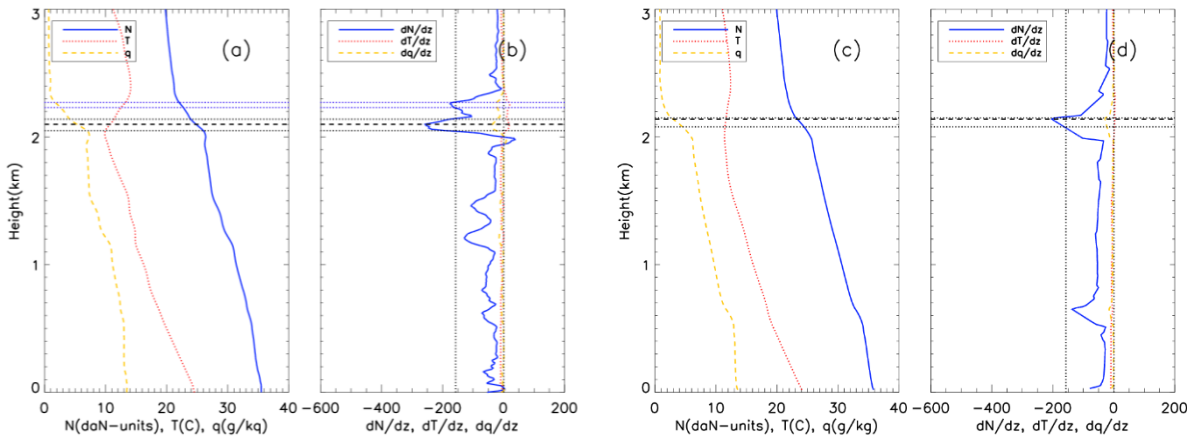
182

183   **Figure 2: Vertical profiles of refractivity (N in da$N$-units, solid blue), temperature (T in ˚C, dotted red) and specific humidity**
184   **(q in g kg^{-1}, dashed gold) for (a) radiosonde at (23.69˚, -150.02˚) launched at 2013-10-02, 05:30 UTC, and (c) colocated ERA5**
185   **at (23.75˚, -150.00˚); and associated gradient profiles for radiosonde (b) and ERA5 (d). The horizontal dashed line highlights**
186   **the height of the minimum gradient, i.e., PBLH. The paired horizontal dotted lines represent the bottom and top of any**
187   **ducting layers.**

188   **2.4 Evaluation of GNSS RO N-bias resulting from ducting**

189   In order to estimate the systematic negative N-bias in GNSS RO observations in the presence of

190   ducting, we use an end-to-end simulation on the radiosonde and ERA5 refractivity profiles. The

191   simulation consists of a two-step process adapted from Xie et al. (2006). The first step is to
192   simulate the 1-dimensional GNSS RO bending angle as a function of impact parameter (i.e., the
193   product of refractive index and the radius of the Earth's curvature) by forward Abel integration of
194   an input refractivity profile assuming a spherically symmetric atmosphere (Fjeldbo and Eshleman,
195   1968; Eshleman, 1973; Sokolovskiy, 2001). The second step is to simulate the spaceborne GNSS
196   RO refractivity retrieval by applying the Abel inversion on the simulated bending angle from step
197   one. In the absence of ducting, the impact parameter increases monotonically with height, allowing
198   a unique solution to the inverse Abel retrieval that is the same as the original refractivity profile
199   input. However, in the presence of an elevated ducting layer, the Abel retrieval systematically
200   underestimates the refractivity profile due to the non-unique Abel inversion problem resulting
201   from the singularity in bending angle across the ducting layer (Sokolovskiy 2003; Xie et al., 2006).
202   It should be noted that after the 100 m vertical smoothing on radiosonde (no smoothing is
203   performed on ERA5) profiles as described in section 2.2, an additional 50 m vertical smoothing
204   has been applied to the simulated bending angle profiles of both radiosonde and ERA5 data sets
205   to alleviate the challenge of integration through the very sharp bending angle resulting from
206   ducting in the inverse Abel integration procedure (Feng et al., 2020).
207   Figure 3 shows the end-to-end simulation results for the same radiosonde (a–d) and the colocated
208   ERA5 (e–h) cases from Fig. 2. Figures 3a and 3e show refractivity profiles from the radiosonde
209   (N_{MAGIC}) and the colocated ERA5 (N_{ERA5}) data as well as their corresponding Abel refractivity
210   retrievals (N_{Abel}). The refractivity gradients are shown in Figures 3c and 3g. The derived PBLH is
211   marked by a horizontal dotted line in the refractivity/height space. The peak bending angles in
212   Figures 3d and 3h are consistent with the corresponding sharp refractivity gradient. Figure 3b
213   shows the fractional N-bias between the simulated Abel retrieved RO refractivity profile and the
214   radiosonde, whereas Figure 3f shows the same for the ERA5 profile. Considering the significant
215   spatial and temporal variations of ducting height along the transect, each N-bias profile is displayed
216   as a function of an adjusted height, which is the height minus the corresponding PBLH for the
217   purposes of profile intercomparison. For example, the zero-adjusted height refers to the PBLH for
218   each individual profile. The systematic negative N-bias is shown below the ducting layer marked
219   by the PBLH in both cases, with the biases decreasing at lower altitude, the largest magnitude bias
220   (−5% for radiosonde; −2.5% for ERA5) close to the ducting height and a minimum magnitude
221   approaching zero near the surface.
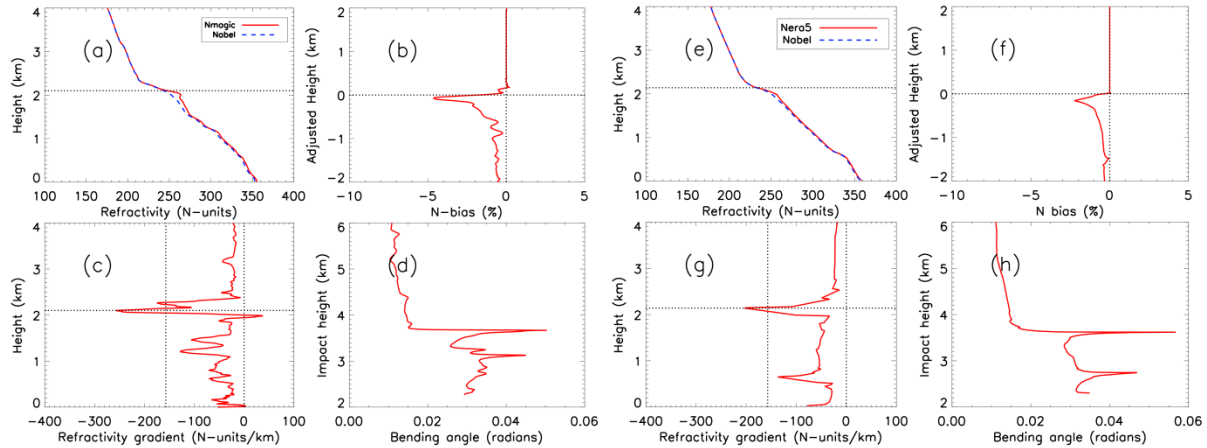
Figure 3: End-to-end simulation results for a MAGIC radiosonde launched at 0530 UTC on 20131002 showing: (a) N_{MAGIC} **(solid red) and** N_{Abel} **(blue dashed) from surface to 4 km; (b) PBLH adjusted** *N*-**bias; (c) vertical refractivity gradient and (d) bending angle vs. impact parameter. Panels e-h show end-to-end simulation results for the colocated ERA5 profile.**

3   Analysis

Quality control for radiosonde (and colocated ERA5) profiles was based on five key criteria. First, a total of 19 radiosonde and 24 ERA5 profiles near the southern California coast were removed due to their positions east of −120˚ or anomalously high PBL (PBLH > 3.0 km) with no distinct minimum gradient. The remaining profiles in the easternmost portion of the domain were too few in number to calculate meaningful statistics. Second, any profile lacking critical refraction (i.e. dN/dz < −157 N-units km^{-1}) points was excluded from the analysis which resulted in the removal of 47 radiosonde and 176 ERA5 profiles. Third, an anomalously noisy bending angle profile could result in errors in Abel refractivity retrieval and cause positive N-bias. Therefore, the profiles with N-bias greater than +0.5% are excluded resulting in the removal of 61 MAGIC profiles and 16 ERA5 profiles. Fourth, the profiles with only surface ducting, i.e., below 300 m threshold, are discarded. Finally, 25 radiosonde profiles and 2 ERA5 profiles were removed due to the Abel retrieval failure. After implementing all quality control measures, the number of radiosonde and ERA5 profiles used for the N-bias analysis is reduced to 396 and 319 profiles, respectively across the MAGIC transect.

3.1 PBL analysis

To evaluate the ducting properties along the transect from the coast of southern California to Hawaii, we group the MAGIC radiosonde and the colocated ERA5 profiles into eight 5˚ longitude

244   bins between −160.0˚ and −120.0˚, which allows for the assessment of the spatial variation of the

245   PBL, ducting layer, and the associated properties along the transect to be easily illustrated. Figure

246   4 shows the median value of PBLH (a), minimum gradient (b) and sharpness parameter (c) along

247   the transect. The median-absolute-deviation (MAD) for each parameter is also shown.

248   In Figure 4a, the MAGIC radiosondes (rds) clearly show a gradual increase of the PBLH along the

249   transect from the shallow stratocumulus-topped PBL (~800 m) near the southern California coast

250   westward to the much deeper trade-cumulus regime (~1.8 km) near Hawaii. A similar structure is

251   seen in the colocated ERA5 data but with an average low bias of 165 m below the radiosonde.

252   Additionally, a nearly 800 m ERA5 underestimation in PBLH over the two westernmost bins near

253   Hawaii is also seen, this is consistent with what is found over the equivalent trade cumulus region

254   of the subtropical southeast Pacific Ocean (Xie et al., 2012). Such a discrepancy could be due to

255   the sensitivity of the gradient method to the vertical resolution of the data. Over the western

256   segment of the transect (near Hawaii), two major gradient layers (one at ~1 km and the other at ~2

257   km) with comparable refractivity gradients are often observed (e.g., Fig. 2) in the ERA5 data. The

258   gradient layer near 2 km is well-known as the trade-wind inversion (Riehl, 1979; Ao et al., 2012;

259   Xie et al., 2012), while the lower-level gradient layer at ~1 km, is generally called a mixing layer

260   (Xie et al., 2006). Due to the differences in vertical sampling noted in Section 2.1, the ERA5 data

261   are more likely to resolve the sharp gradient structure below 1 km than the one at higher altitude.

262   This could result in resolving the mixing layer (below 1 km) with the sharpest refractivity gradient,

263   instead of the trade-wind inversion near 2 km in the ERA5 data. Note that the larger median

264   absolute deviation for the westernmost bins compared to the rest of the transect illustrates the

265   existence of greater PBLH variability closer to the trade-cumulus boundary layer regime. The

266   westward decreasing magnitude of the minimum refractivity gradient (Fig. 4b) and sharpness

267   parameter (Fig. 4c) indicates the westward weakening of moisture lapse rate and/or temperature

268   inversion across the PBL top, which is consistent with the decreasing synoptic-scale subsidence

269   from the California coast to Hawaii (Riehl, 1979).
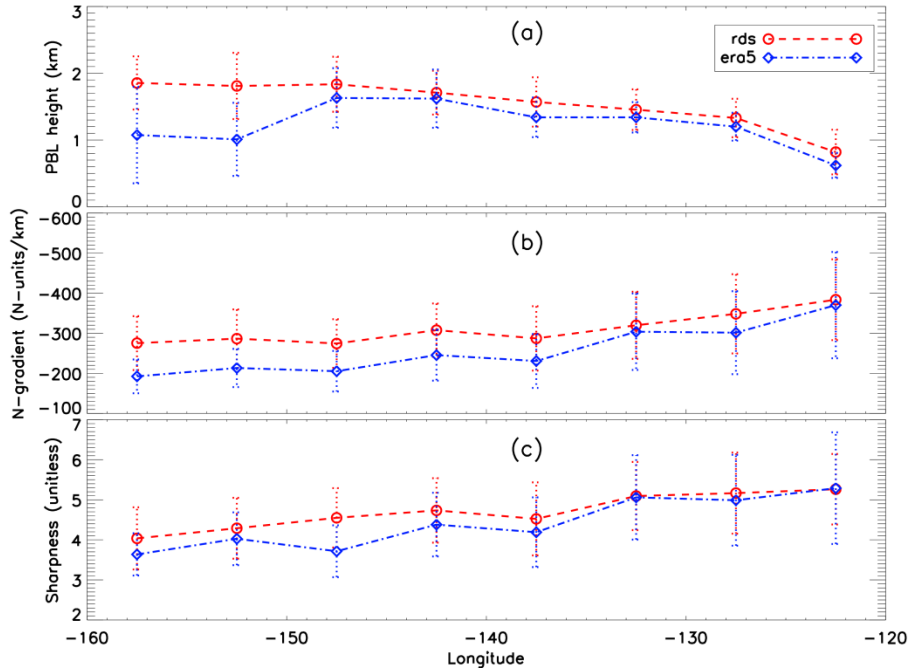
Figure 4: Zonal transect of 5° binned MAGIC and ERA5 PBLH (a), minimum refractivity gradient and (b) sharpness parameter (c) for MAGIC (median in red circle and dashed line, MAD in red dotted error bars) and ERA5 (median in blue diamond and dot-dashed line, MAD in blue dotted error bars).

It is also notable that the ERA5 systematically underestimates not only the PBLH but also the magnitude of the minimum gradient across the entire transect. This can also be seen in the sharpness parameter west of −132.5°. This discrepancy could be partially attributed to the decrease in vertical sampling in ERA5 profiles as compared to the radiosondes, the result of which leads to a weaker PBL refractivity gradient and coincides with an increasing PBLH. Therefore, the underestimation of the ERA5 minimum refractivity gradient increases in magnitude from east to west and becomes most prominent near Hawaii where the PBLH reaches the maximum over the region.

3.2 Ducting characteristics

As introduced in Sect. 2.3, the key characteristics of the ducting layer along the transect will be investigated. These characteristics include the ducting layer height, ducting layer thickness (Δh), and ducting strength (ΔN), as well as the average refractivity gradient within the ducting layer ($\Delta N/\Delta h$). The ducting layer heights from both radiosondes and ERA5 show a westward increase along the transect, as seen in Figure 5a. Note again that the ERA5 shows a systematic ~100–200 m low bias when compared to the radiosondes between −122.5° and −147.5°, with the difference

290   increasing to more than 500 m near Hawaii. The ducting layer thickness is the median height from

291   the bottom of the ducting layer to the top and is expressed in km (Fig. 5b). Ducting thickness (Δh)

292   for MAGIC shows a near constant value of 110 m across the entire transect with only a slight

293   increase to 130 m at $-122.5°$, consistent with Ao et al. (2003). Conversely, the ERA5 shows a

294   constant but slightly thicker ducting layer to the east of $-137.5°$ and then a decreasing thickness to

295   the west of $-137.5°$ (Fig. 5b). It should be noted that the estimated thicknesses of the ducting

296   layers, especially for ERA5, may be affected by the chosen interpolation method.

297   The ducting layer strength is the decrease in refractivity from the bottom of the ducting layer to

298   the top (Fig. 5c) and the ratio $\Delta N/\Delta h$ reflects the average gradient of the ducting layer (Fig. 5d).

299   The ducting strength (ΔN) for the radiosondes generally ranges from 25 N-units near Hawaii to 40

300   N-units near the coast of California. Both ΔN and $\Delta N/\Delta h$ show an overall westward decreasing

301   trend along the transect which is consistent with the decrease in magnitude of the refractivity

302   gradient (Fig. 4b). Note that MAGIC and ERA5 show similar ducting strength in the eastern part

303   of the region but diverge near $-137.5°$ with ERA5 10 to 20 N-units weaker than the MAGIC

304   profiles. On the other hand, ERA5 shows a systematically lower average refractivity gradient

305   ($\Delta N/\Delta h$) than MAGIC throughout the transect, indicating the challenge in ERA5 to consistently

306   resolve the sharp vertical structure in refractivity, and likewise in temperature and moisture

307   profiles, across such a thin ducting layer. The problem becomes acutely clear near the trade

308   cumulus region.

309

310
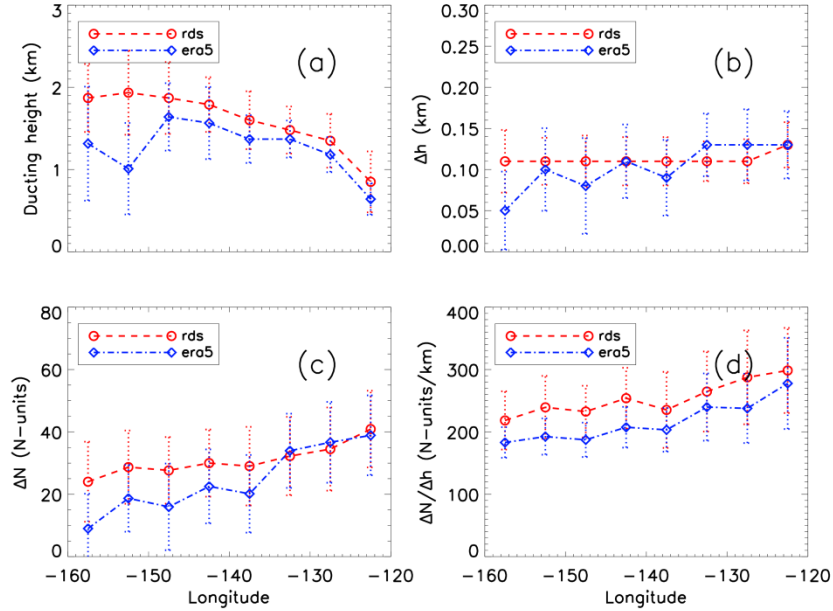
311
312 **Figure 5: Zonal transect of 5° binned median (a) ducting height, (b) ducting layer thickness (Δ*h*), (c) ducting layer strength**
313 **(Δ*N*), and (d) average ducting layer gradient Δ*N*/Δ*h* for MAGIC (median in red circle and red-dashed line, MAD in red-**
314 **dotted error bars) and ERA5 (median in blue diamond and dot-dashed line, MAD in blue-dotted error bars).**
315

316 Figure 6 shows individual ducting layer thicknesses as a function of ducting layer strength. The

317 shape and color of each data point is used to identify its respective longitude bin. The relationship

318 between Δ*h* and Δ*N* is not longitude-dependent for either data set, but a linear trend is evident for

319 thinner ducting layers (Δ*h* < 0.1 km) with weaker ducting strength (Δ*N* < ~25 N-units). However,

320 for the ducting layers thicker than 0.1 km, such a trend becomes less identifiable, and the ducting

321 strength Δ*N* begins to show more variability toward larger values.

322
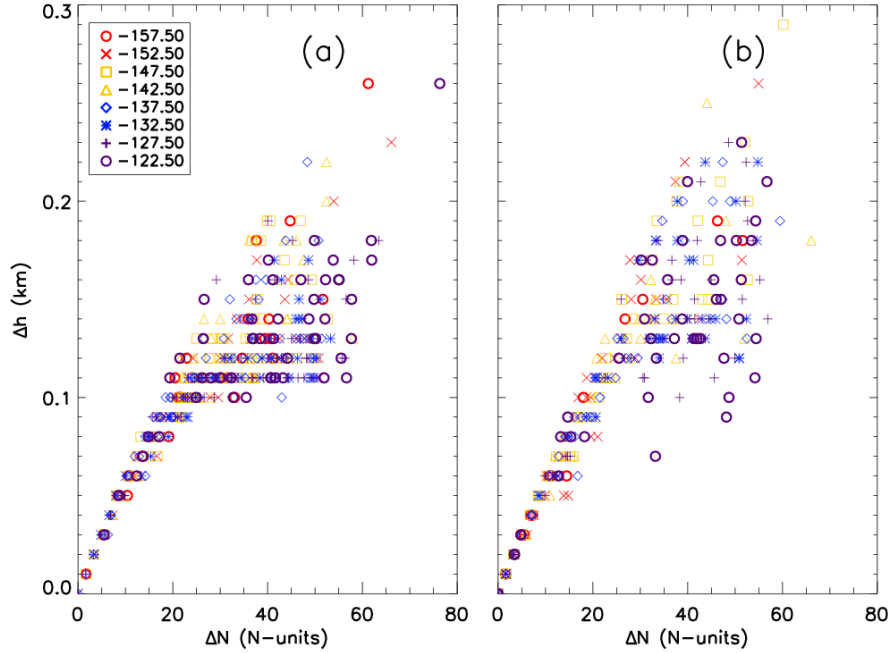
323
324 **Figure 6: Comparison of individual profiles' ducting strength (Δ*N*) vs. ducting thickness (Δ*h*) for MAGIC (a) and ERA5**
325 **(b). The shape and color of each character represents the location of the 5° longitude bin of each observation.**

3.3 Ducting-induced GNSS RO *N*-bias statistics

To estimate the systematic negative *N*-bias in GNSS RO observations due to ducting, we have applied the end-to-end simulation described in Sect. 2.4 to all radiosonde and ERA5 refractivity profiles with at least one elevated ducting layer detected. The *N*-bias along the transect as well as its relationship to the ducting properties are presented below.

3.3.1 Assessing ducting-induced *N*-bias

Figure 7 shows a composite of both MAGIC (396 profiles) and ERA5 (319 profiles) *N*-bias profiles which have been displayed as a function of their zero-adjusted height. The median *N*-bias and MAD are also shown. The systematic negative *N*-bias peaks at approximately 100 m below the PBLH and decreases at lower relative altitudes. The peak median value of the *N*-bias for radiosondes is −5.42% (MAD, 2.92%), nearly twice the ERA5 value of −2.96% (MAD, 2.59%), indicating the significant underestimation of ducting strength in ERA5 data. However, the MAD of the radiosonde and ERA5 data are within 0.33% of each other, indicating that ERA5 data successfully capture the variations of ducting features seen in the radiosondes. It is worth noting that many radiosonde profiles show small negative *N*-biases above the PBLH (i.e., positive zero-

341 adjusted height), which is the result of a secondary ducting layer above the major ducting layer

342 near the PBLH. Few ERA5 profiles show the presence of the secondary ducting layer above PBLH.

343
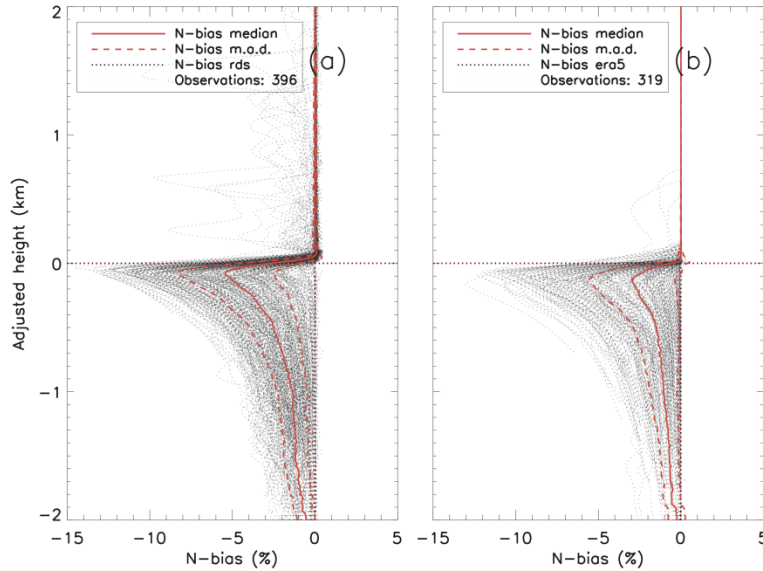
344
345 **Figure 7: Fractional refractivity difference (*N*-bias) between the simulated Abel-retrieved refractivity profile and the**
346 **original observed refractivity profile for all individual observations (dotted gray): (a) MAGIC radiosondes (396 total**
347 **profiles) and (b) ERA5 (319 total profiles) with population median (solid red) ± MAD (dashed red). Note the zero value in**
348 **the adjusted height refers to the detected PBLH for each individual *N*-bias profile.**

349 ### 3.3.2 Zonal variation of the *N*-bias along the transect

350 To illustrate the large variation in the *N*-bias vertical structure resulting from the spatial variations

351 of ducting height and strength, Figure 8 shows the median *N*-bias profiles (± MAD) for each 5°

352 bin, replacing the zero adjusted height with the median PBLH for each bin. The zonal radiosonde

353 composite (Fig. 8a) illustrates the westward transition of the median *N*-bias profiles from the

354 largest peak *N*-bias at ~0.8 km near the coast of Los Angeles, California, to a much-reduced peak

355 *N*-bias but higher altitude of ~1.8 km at Honolulu, Hawaii. Table 1 lists detailed statistics of the

356 peak *N*-bias values at each bin for both radiosonde and ERA5 data seen in Fig. 8. Although the

357 vertical structure of the *N*-bias profiles along the transect are consistent as seen in Fig. 7, significant

358 changes of the *N*-bias magnitude and its peak height along the transect are seen.

359 The maximum peak *N*-bias (−7.86%) in the radiosonde data is located at the easternmost of the

360 transect near California (−122.5˚), whereas the minimum peak *N*-bias (−4.37%) is located near the

361 center of the transect (−147.5˚). Similarly, the ERA5 also show the maximum peak *N*-bias

362 (−5.92%) near California (−122.5˚). However, the minimum peak *N*-bias (−0.77%) is found near

363   Hawaii (−157.5˚). Overall, the *N*-bias values for the ERA5 data set are less than the *N*-bias values

364   calculated from the radiosonde data set for each longitude bin. However, a noticeable difference

365   exists between the ERA5 and radiosonde profiles for the two westernmost longitude bins (−157.5˚

366   and −152.5˚) where the ERA5 reveals a much lower and weaker *N*-bias than the MAGIC data.

367   The PBLH is above the height of the peak *N*-bias for both data sets. The MAGIC data show a

368   maximum difference of 100 m (−157.5˚) and a minimum difference of ~70 m (−142.5˚) while the

369   ERA5 PBLH shows greater values for maximum difference (140 m at −132.5˚) and minimum

370   difference (60 m at −157.5˚).

371
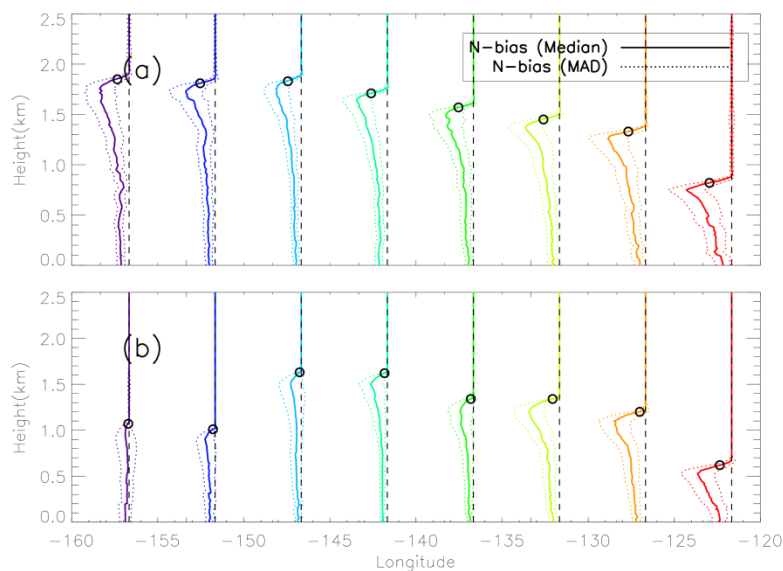
Figure 8: Median *N*-bias (solid) ± MAD (dotted) *N*-bias along the north Pacific transect for MAGIC radiosondes (a) and
ERA5 (b). Open circles represent the median PBLH for each 5˚ bin. Vertical dashed line represents the location of each 5˚
grid bin. See Table 1 for corresponding values of median and M.A.D. peak *N*-bias.

Table 1: Peak values of median *N*-bias and corresponding MAD (%) values for MAGIC radiosondes (RDS) and ERA5 for
each 5˚ bin seen in Figure 8.

Peak N-bias (%)				
Longitude	RDS median	RDS MAD	ERA5 median	ERA5 MAD
−157.5˚	−5.12	±2.61	−0.77	±1.73
−152.5˚	−5.10	±2.97	−1.76	±1.61
−147.5˚	−4.37	±2.14	−1.83	±2.10
−142.5˚	−5.36	±2.53	−2.95	±2.17
−137.5˚	−4.82	±2.96	−2.31	±2.14
−132.5˚	−5.90	±3.03	−5.31	±2.68
−127.5˚	−6.55	±3.40	−5.45	±2.88
−122.5˚	−7.86	±3.15	−5.92	±3.04

379
380

381   Figure 9 further illustrates the peak N-bias, median PBL N-bias (0.3 km to PBLH), and the near
382   surface N-bias (at 0.3 km) at each bin along the transect. Note the median PBL N-bias refers to the
383   median value from the near-surface (0.3 km) to the PBLH. Contrary to the general trend of
384   westward decrease in magnitude of the minimum refractivity gradient (Fig. 4b) and ducting
385   strength (Fig. 5c), the radiosonde peak N-bias (median: −8.10%, MAD: 3.26%) occurs near
386   California (−122.5°) and the minimum (median: −4.85%, MAD: 2.18%) occurs over the transition
387   region (−147.5°). There is also a slight increase in peak N-bias to a secondary maximum (median:
388   −6.11%, MAD: 2.85%) near Hawaii (−157.5°). The median PBL N-bias and the near surface N-
389   bias also show a similar pattern. However, the median N-bias demonstrates a sharp decrease in the
390   eastern half of the domain from −5.25% (MAD: 2.71%) at −122.5° to −1.71% (MAD: 1.26%) at
391   −137.5°, and then remains relatively constant over the western half of the domain. Similarly, the
392   near surface N-bias reaches a maximum magnitude of −3.54% (MAD: 2.11%), sharply decreases
393   to −1.06% (MAD: 0.85%) at −137.5°, and then remains relatively constant over the western half
394   of the domain. Note that normalizing each N-bias profile to the PBLH preserves the magnitude of
395   the N-bias with various heights. Therefore, the relatively large, normalized N-biases observed near
396   Hawaii indicates more persistent ducting over the trade-cumulus boundary layer regime compared
397   to the transition region in the middle of the transect at -147.5° (Fig. 8a).
398   On the other hand, the ERA5 data show a westward decrease of all three N-biases, systematically
399   underestimating all three as compared to the radiosondes. This is expected as the decrease of ERA5
400   vertical resolution at higher altitude leads to a weaker PBL N-gradient observation (Fig. 4b), and
401   thus weaker ducting and a smaller ducting-induced N-bias. Such underestimation of the N-bias in
402   the ERA5 reanalysis minimizes near California where the PBLH is lowest but becomes more
403   severe westward with an increase in height, reaching a maximum magnitude N-bias difference
404   near Hawaii. In this case, the peak N-bias is merely −0.71% (MAD: 1.80%) as compared to −6.23%
405   (MAD: 2.98%) at −122.5° (Fig. 9a). The large difference seen in the N-bias along the transect
406   strongly indicates the challenges of the ERA5 data to resolve the sharp gradient across the ducting
407   layer, resulting in a large variation in PBLH of the ERA5 data in the western segment of the region.
408   The increasing difference between the radiosonde and ERA5 data from east to west is most
409   pronounced in the peak N-bias cross-section (Fig. 9a) but is also evident in both the median N-bias
410   (Fig. 9b) as well as the near surface N-bias (Fig. 9c).
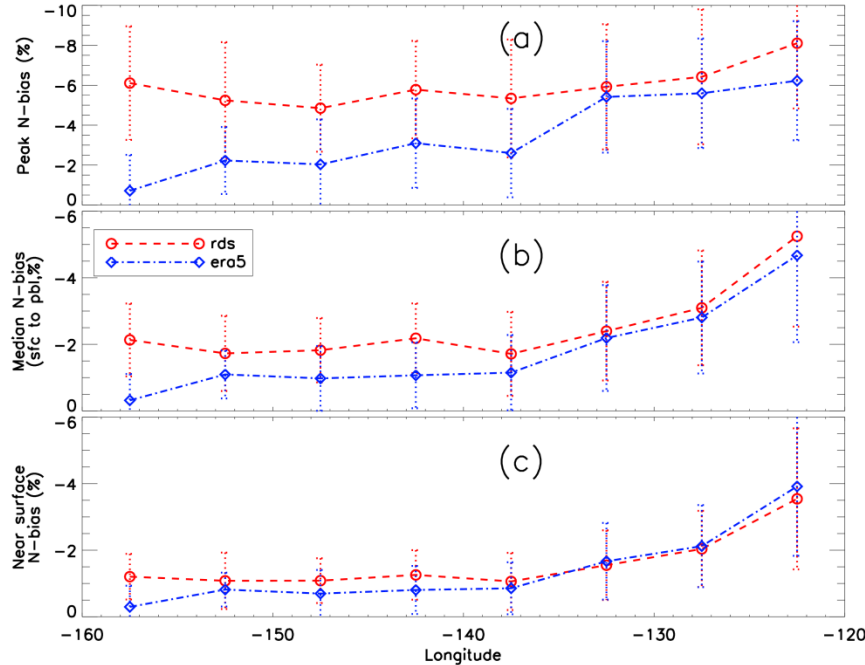
411
412 **Figure 9: Zonal transect of 5° binned (a) peak *N*-bias, (b) median PBL *N*-bias (0.3 km to PBLH), and (c) near surface *N*-**
413 **bias at 0.3 km for MAGIC (median in red circle and red-dashed line, MAD in red-dotted error bar) and ERA5 (median in**
414 **blue diamond and dot-dashed line, MAD in blue-dotted error bar)**

4   Summary and Conclusions

415

416 In this study, radiosonde profiles from the MAGIC field campaign have been analyzed to

417 investigate ducting characteristics and the induced systematic refractivity biases in GNSS RO

418 retrievals over the Northeastern Pacific Ocean between Hawaii and California. Colocated ERA5

419 model reanalysis data were used as a secondary comparison to the radiosonde observations.

420 The nearly 1-year high-resolution MAGIC radiosonde data set reveals the frequent presence of

421 ducting marked by a sharp refractivity gradient resulting from the large moisture lapse rate across

422 a strong temperature inversion layer. The PBLH increases by more than 1 km along the transect

423 from California to Hawaii, while the magnitude of the refractivity gradient decreases by 100 N-

424 units km^{-1}. The zonal gradient of both variables illustrates the transition of the PBL from shallow

425 stratocumulus adjacent to the California coast to deeper trade-wind cumulus that are prevalent near

426 the Hawaiian Islands.

427 End-to-end simulations on all radiosonde and ERA5 refractivity profiles have been conducted to

428 estimate the systematic negative *N*-bias in GNSS RO observations. The ducting layer maintains

429 remarkably consistent thickness (~110 m) along the transect with westward decreasing strength

430 and increasing height. The ERA5 slightly underestimates both the height and strength of the

ducting layer as well as the PBLH. A systematic negative *N*-bias below the ducting layer is observed throughout the transect, peaking (−5.42%) slightly below the PBLH, and gradually decreasing towards the surface (−0.5%).

MAGIC radiosondes indicate larger values of both ducting strength (ΔN) and thickness (Δh) than ERA5 in the western half of the transect. The opposite is true in the eastern portion of the domain and is likely associated with the transition of the cloud layer from open-cell cumulus in the west to stratocumulus and stratus in the east (Wood et al., 2011; Bretherton et al., 2019). ERA5 systematically underestimates the average ducting layer gradient ($\Delta N/\Delta h$) comparing to the radiosondes. The largest *N*-bias is found over the region with strongest ducting and largest sharpness parameter. It is worth noting that the PBL over the western portion of the transect near Hawaii frequently shows two major gradient layers (a mixing layer at ~1 km and the trade-inversion at ~2 km), with comparable *N*-gradients (e.g., Fig. 2). The much lower PBLH seen in ERA5 in this region is likely due, in part, to the decreasing number of model levels in ERA5 at higher altitude, which could lead to a higher possibility of identifying the lower gradient layer as the PBLH. However, the impact of the vertical resolution and on the performance of the gradient method for PBLH detection has not been performed in this study. Further, the ERA5 results may be affected by the interpolation resolution and gradient are calculation. Both warrant a more comprehensive study in the future.

5   Data availability

Data for the Marine Atmospheric Radiation Measurement (ARM) GCSS Pacific Cross Section Intercomparison (GPCI) Investigation of Clouds (MAGIC, Zhou et al., 2015) can be accessed through the U.S. Department of Energy's Office of Science https://www.arm.gov/research/campaigns/amf2012magic.

Data for the ECMWF Reanalysis version 5 (ERA5, Hersbach et al., 2020) can be accessed at https://www.ecmwf.int/en/forecasts/dataset/ecmwf-reanalysis-v5.

6   Author contribution

Author Thomas Winning is responsible for all original text data analysis, and production of graphics. Author Kevin Nelson contributed by providing updated data processing and end-to-end

459   simulation code, colocation of ERA5 data with MAGIC observations, and manuscript edits.

460   Author Feiqin Xie is the academic advisor for the primary author and also provided draft edits and

461   paper organization and writing guidance.

462

463 **7   Competing interests**

464   The authors declare no competing interests, see Acknowledgements for current affiliations.

465 **8   Acknowledgements**

466   The authors acknowledge funding support of earlier work from NASA grant (NNX15AQ17G).

467   Authors T. Winning and K. Nelson were also partially supported by research assistantships from

468   the Coastal Marine System Science Program at Texas A&M University – Corpus Christi. The

469   high-resolution ERA5 reanalysis data were acquired from ECMWF and the Climate Data Service

470   (CDS). The MAGIC radiosonde data were provided by the Atmospheric Radiation Measurement

471   program (ARM) Climate Research Facility sponsored by the U.S. Department of Energy (DOE).

472   Author K. Nelson's current affiliation: Jet Propulsion Laboratory, California Institute of

473   Technology, Pasadena, CA, 91109, USA. Author K. Nelson acknowledges this work was done as

474   a private venture and not in the author's capacity as an employee of the Jet Propulsion Laboratory,

475   California Institute of Technology.

476

477

478

479

480

481

482

483

484 **References**

485 Anthes, R. A., and Coauthors: The COSMIC/FORMOSAT-3 Mission: Early Results, BAMS, 89, 313–334,
486 doi.org/10.1175/bams-89-3-313, 2008.
487

488 Ao, C. O., Meehan T. K., Hajj, G. A., Mannucci, A. J., and Beyerle, G.: Lower Troposphere Refractivity Bias in GPS
489 Occultation Retrievals, J. Geophys. Res., 108, 4577, doi:10.1029/2002JD003216, 2003.
490

491 Ao, C. O.: Effect of Ducting on Radio Occultation Measurements: An Assessment Based on High-resolution
492 Radiosonde Soundings, Radio Sci., 42, RS2008, doi.org/10.1029/2006RS003485, 2007.
493

494 Ao, C. O., Chan, T. K., Iijima, A., Li, J.-L., Mannucci, A. J., Teixeira, J., Tian, B., and Waliser, D. E.: Planetary
495 Boundary Layer Information from GPS Radio Occultation Measurements, in: Proceedings of the GRAS SAF
496 Workshop on Applications of GPSRO Measurements, Vol. 5 of, GRAS SAF Workshop on Applications of GPSRO
497 Measurements, Reading, United Kingdom, ECMWF and EUMETSAT, 123–131,
498 https://www.ecmwf.int/sites/default/files/elibrary/2008/7459-planetary-boundary-layer-information-gps-radio-
499 occultation-measurements.pdf, 16–18 June, 2008.
500

501 Ao, C. O., Waliser, D. E., Chan, S. K., Li, J.-L., Tian, B., Xie, F., and Mannucci, A. J.: Planetary boundary layer
502 heights from GPS radio occultation refractivity and humidity profiles, J. Geophys. Res., 117, D16117,
503 doi:10.1029/2012JD017598, 2012.
504

505 Basha, G., and Ratnam, M. V.: Identification of atmospheric boundary layer height over a tropical station using high-
506 resolution radiosonde refractivity profiles: Comparison with GPS radio occultation measurements, J. Geophys. Res.,
507 114, doi.org/10.1029/2008jd011692, 2009.
508

509 Beyerle, G., Gorbunov, M. E., and Ao, C.O.: Simulation studies of GPS radio occultation measurements, Radio Sci.,
510 38, 1084, doi:10.1029/2002RS002800, 2003.
511

512 Bretherton, C.S., and Coauthors: Cloud, Aerosol, and Boundary Layer Structure across the Northeast Pacific
513 Stratocumulus–Cumulus Transition as Observed during CSET, Mon.Wea. Rev., 147, 2083–2102. DOI:
514 10.1175/MWR-D-18-0281, 2019
515

516 Eshleman, V.R.: The radio occultation method for the study of planetary atmospheres, Planet. Space Sci., 21, 1521-
517 1531, doi.org/10.1016/0032-0633(73)90059-7, 1973.
518

519 Feng, X., Xie, F., Ao, C.O., and Anthes, R.A.: Ducting and Biases of GPS Radio Occultation Bending Angle and
520 Refractivity in the Moist Lower Troposphere, J. Atmos. Oceanic Technol., 37, 1013–1025, doi.org/10.1175/JTECH-
521 D-19-0206.1, 2020.

522

523 Fjeldbo, G., and Eshleman, V.R.: The Atmosphere of Mars Analyzed by Integral Inversion of the Mariner IV
524 Occultation Data, Planet. Space Sci., 16, 1035-1059, doi.org/10.1016/0032-0633(68)90020-2, 1968.

525

526 Fjeldbo, G., Kliore, A.J., and Eshleman, V.R.: The Neutral Atmosphere of Venus as Studied with the Mariner V Radio
527 Occultation Experiment, Astron. J., 76, 123-140, doi.org/10.1086/111096, 1971.

528

529 Garratt, J. R.: Review: the atmospheric boundary layer, Earth-Sci. Rev., 37, 89–134, 1994

530

531 Guo, P., Kuo, Y. H., Sokolovskiy, S. V., and Lenschow, D. H.: Estimating Atmospheric Boundary Layer Depth Using
532 COSMIC Radio Occultation Data, J. Atmos. Sci., 68, 1703–1713, doi.org/10.1175/2011jas3612.1, 2011.

533

534 Gorbunov, M. E.: Canonical transform method for processing radio occultation data in the lower troposphere, Radio
535 Sci., 37(5), 1076, doi:10.1029/2000RS002592, 2002.

536
537 Gorbunov, M. E., Benzon, H. H., Jensen, A.S, Lohmann, M.S., and Nielsen, A.S.: Comparative analysis of radio
538 occultation processing approaches based on Fourier integral operators. Radio Sci., 39, RS6004,
539 https://doi.org/10.1029/2003RS002916, 2004

540

541 Healy, S. B.: Radio occultation bending angle and impact parameter errors caused by horizontal refractive index
542 gradients in the troposphere: A simulation study, J. Geophys. Res, 106, D11, 11875–11889,
543 doi:10.1029/2001JD900050, 2001.

544

545 Hersbach, H., Bell, B., Berrisford, P., Hirahara, S., Horányi, A., Muñoz-Sabater, J., Nicolas, J., Peubey, C., Radu, R.,
546 Schepers, D., Simmons, A., Soci, C., Abdalla, S., Abellan, X., Balsamo, G., Bechtold, P., Biavati, G., Bidlot, J.,
547 Bonavita, M., De Chiara, G., Dahlgren, P., Dee, D., Diamantakis, M., Dragani, R., Flemming, J., Forbes, R., Fuentes,
548 M., Geer, A., Haimberger, L., Healy, S., Hogan, R. J., Hólm, E., Janisková, M., Keeley, S.,
549 Laloyaux, P., Lopez, P., Lupu, C., Radnoti, G., de Rosnay, P., Rozum, I., Vamborg, F., Villaume, S., and Thépaut, J.-
550 N.: The ERA5 Global Reanalysis, Q. J. Roy. Meteor. Soc., 146, 1999–2049, https://doi.org/10.1002/qj.3803, 2020.

551
552 Ho, S.-P., Peng, L., Anthes, R. A., Kuo, Y.-H., and Lin, H.-C.: Marine boundary layer heights and their longitudinal,
553 diurnal and inter-seasonal variability in the southeast Pacific using COSMIC, CALIOP, and radiosonde data. J.
554 Climate, 28, 2856–2872, https://doi.org/10.1175/JCLI-D-14-00238.1, 2015.

555

556   Jensen, A. S., Lohmann, M.S., Nielsen, A.S. and Benzon, H.-H.: Geometrical optics phase matching of radio

557   occultation signals, Radio Sci., 39, RS3009, doi:10.1029/2003RS002899, 2004.

558

559   Jensen, A. S., Lohmann, M.S., Benzon, H.-H, and Nielsen, A.S.: Full spectrum inversion of radio occultation signals,

560   Radio Sci., 38(3), 1040, doi:10.1029/2002RS002763, 2003.

561

562   Johnston, B. R., Xie, F., and Liu, C.: The effects of deep convection on regional temperature structure in the tropical

563   upper troposphere and lower stratosphere, J. Geophys. Res.: Atmos., 123, 1585−1603,

564   doi.org/10.1002/2017JD027120, 2018.

565

566   Klein, S. A., and Hartmann, D. L.: The seasonal cycle of low stratiform clouds. Journal of Climate, 6, 1587−1606,

567   doi:10.1175/1520-0442(1993)006<1587:TSCOLS>2.0.CO;2, 1993.

568

569   Kursinski, E. R., Hajj, G. A., Schofield, J. T., Linfield, R. P., and Hardy, K. R.: Observing Earth's atmosphere with

570   radio occultation measurements using the Global Positioning System, J. Geophys. Res.: Atmos., 102, 23429−23465,

571   doi.org/10.1029/97jd01569, 1997.

572

573   Kursinski, E. R., G. A. Hajj, Leroy, S. S., and Herman, B.: The GPS Radio Occultation Technique. Terr. Atmos.

574   Ocean. Sci. (TAO), 11, 53−114, 2000.

575

576   Lewis, E. R.: Marine ARM GPCI Investigation of Clouds (MAGIC) Field Campaign Report. U.S. Department of

577   Energy, https://doi.org/10.2172/1343577, 2016.

578

579   Maddy, E. S. and Barnet, C. D.: Vertical resolution estimates in version 5 of AIRS operational retrievals. IEEE

580   Transactions on Geoscience and Remote Sensing, 46, 2375−2384, doi:10.1109/TGRS.2008.917498, 2008.

581

582   Nelson, K. J., Xie, F., Ao, C. O., and Oyola-Merced, M. I.: Diurnal Variation of the Planetary Boundary Layer Height

583   Observed from GNSS Radio Occultation and Radiosonde Soundings over the Southern Great Plains. J. Atmos.

584   Oceanic Tech., 38, 2081−2093, https://doi.org/10.1175/jtech-d-20-0196.1, 2021.

585

586   Nelson, K. J., Xie, F., Chan, B. C., Goel, A., Kosh, J., Reid, T. G. R., Snyder, C. R., and Tarantino, P. M.: GNSS

587   Radio Occultation Soundings from Commercial Off-the-Shelf Receivers Onboard Balloon Platforms, Atmos. Meas.

588   Tech., https://doi.org/10.5194/amt-2022-198, 2022.

589

590   Painemal, D., Minnis, P., and Nordeen, M.: Aerosol variability, synoptic-scale processes, and their link to the cloud

591   microphysics over the northeast Pacific during MAGIC, J. Geophys. Res. Atmos., 120, 5122−5139,

592   doi:10.1002/2015JD023175, 2015.

593

Patterson, W. L.: Climatology of Marine Atmospheric Refractive Effects: A Compendium of the Integrated Refractive Effects Prediction System (IREPS) Historical Summaries. Naval Ocean Systems Center, https://apps.dtic.mil/sti/pdfs/ADA155241.pdf, 1982.

Ramanathan, V., Cess, R. D., Harrison, E. F., Minnis, P., Barkstrom, B. R., Ahmad, E., and Hartmann, D.: Cloud-radiative forcing and climate: Results from the Earth Radiation Budget Experiment, Science, 243, 57–63, DOI:10.1126/science.243.4887.57, 1989.

Riehl, H.: Climate and weather in the tropics. London: Academic Press. 611 pp. ISBN 0.12.588180.0

Rocken, C., Anthes, R., Exner, M., Hunt, D., Sokolovskiy, S., Ware, R., Gorbunov, M., Schreiner, W., Feng D., Herman B., Kuo, Y.-H., Zou, X.: Analysis and validation of GPS/MET data in the neutral atmosphere. J. Geophys. Res., 102, 29849−29866, https://doi.org/10.1029/97JD02400, 1997.

Schreiner, W. S., Weiss, J.P., Anthes, R.A., Braun, J., Chu, V., Fong, J., Hunt, D., Kuo, Y.-H., Meehan, T., Serafino, W., Sjoberg, J., Sokolovskiy, C., Talaat, E., Wee, T.K., Zeng, Z.: COSMIC-2 Radio Occultation Constellation: First Results. Geophys. Res. Lett., 47, https://doi.org/10.1029/2019gl086841, 2020.

Seidel, D. J., Ao, C.O. and Li, K.: Estimating climatological planetary boundary layer heights from radiosonde observations: Comparison of methods and uncertainty analysis, J. Geophys. Res., 115, D16114, doi:10.1029/2009JD013680, 2010.

Smith, E. K. and Weintraub, S.: The Constants in the Equation for Atmospheric Refractivity Index at Radio Frequencies. Proc. IRE, 41, 1035−1037, doi:10.1109/JRPROC.1953.274297, 1953.

Sokolovskiy, S. V.: Modeling and Inverting Radio Occultation Signals in the Moist Troposphere. Radio Sci., 36, 441−458, https://doi.org/10.1029/1999RS002273, 2001.

Sokolovskiy, S. V.: Effect of super refraction on inversions of radio occultation signals in the lower troposphere. Radio Sci., 38 (3), https://doi.org/10.1029/2002RS002728, 2003.

Sokolovskiy, S. V., Kuo, Y.-H., Rocken, C., Schreiner, W. S., Hunt, D. and Anthes, R. A., 2006: Monitoring the atmospheric boundary layer by GPS radio occultation signals recorded in the open-loop mode. Geophys. Res. Lett., 33, L12813, doi:10.1029/2006GL025955, 2006.

Stull, R., Santoso, E., Berg, L. K., and Hacker, J.: Boundary Layer Experiment 1996 (BLX96), BAMS, 78, 1149−1158, doi: 10.1175/1520-0477(1997)078<1149:BLEB>2.0.CO;2, 1997.

Stull, R. B.: An Introduction to Boundary Layer Meteorology. Kluwer Academic Publishers, 666 pp., ISBN 90-277-2768-6, 1988.

von Engeln, A. and Teixeira, J.: A Planetary Boundary Layer Height Climatology Derived from ECMWF Reanalysis Data, J. Climate, 26, 6575−6590, https://doi.org/10.1175/jcli-d-12-00385.1, 2013.

Winning, T. E., Chen, Y.-L., and Xie, F.: Estimation of the marine boundary layer height over the central North Pacific using GPS radio occultation, Atmospheric Research, 183, 362−370, https://doi.org/10.1016/j.atmosres.2016.08.005, 2017.

Wood, R., Mechoso, C. R., Bretherton, C. S., Weller, R. A., Huebert, B., Straneo, F., Albrecht, B. A., Coe, H., Allen, G., Vaughan, G., Daum, P., Fairall, C., Chand, D., Gallardo Klenner, L., Garreaud, R., Grados, C., Covert, D. S., Bates, T. S., Krejci, R., Russell, L. M., de Szoeke, S., Brewer, A., Yuter, S. E., Springston, S. R., Chaigneau, A., Toniazzo, T., Minnis, P., Palikonda, R., Abel, S. J., Brown, W. O. J., Williams, S., Fochesatto, J., Brioude, J., and Bower, K. N.: The VAMOS Ocean-Cloud-Atmosphere-Land Study Regional Experiment (VOCALS-REx): goals, platforms, and field operations, Atmos. Chem. Phys., 11, 627−654, https://doi.org/10.5194/acp-11-627-2011, 2011.

Xie, F., Syndergaard, S., Kursinski, E. R., and Herman, B.M.: An Approach for Retrieving Marine Boundary Layer Refractivity from GPS Occultation Data in the Presence of Super-refraction. J. Atmos. Oceanic Technol., 23, 1629−1644, https://doi.org/10.1175/JTECH1996.1, 2006.

Xie, F., Haase, J. S., and Syndergaard, S.: Profiling the Atmosphere Using the Airborne GPS Radio Occultation Technique: A Sensitivity Study. IEEE Transactions on Geoscience and Remote Sensing, 46, 3424−3435, https://doi.org/10.1109/tgrs.2008.2004713, 2008.

Xie, F., Wu, D. L., Ao, C. O., Kursinski, E. R., Mannucci, A. J., and Syndergaard, S.: Super-refraction effects on GPS radio occultation refractivity in marine boundary layers, Geophys. Res. Lett., 37, https://doi.org/10.1029/2010gl043299, 2010.

Xie, F., Wu, D. L., Ao, C. O., Mannucci, A. J., and Kursinski, E. R.: Advances and limitations of atmospheric boundary layer observations with GPS occultation over southeast Pacific Ocean, Atmos. Chem. Phys., 12, 903−918, doi:10.5194/acp-12-903-2012, 2012.

Zhou, X., Kollias, P., and Lewis, E.: Clouds, precipitation and marine boundary layer structure during MAGIC. J. Climate, 28, 2420−2442, https://doi.org/10.1175/JCLI-D-14-00320.1, 2015.